Synthesis and physical properties of single-crystalline InTe: towards high thermoelectric performance

Shantanu Misra, Petr Levinský, Anne Dauscher, Ghouti Medjahdi, Jiří Hejtmánek, Bernard Malaman, G. Jeffrey Snyder, Bertrand Lenoir, Christophe Candolfi

Synthesis and physical properties of single-crystalline InTe: Towards high thermoelectric performance

Shantanu Misra[1], Petr Levinský[2], Anne Dauscher[1], Ghouti Medjahdi[1], Jiří Hejtmánek[2], Bernard Malaman[1], G. Jeffrey Snyder[3], Bertrand Lenoir[1], Christophe Candolfi[1,*]

[1] *Institut Jean Lamour, UMR 7198 CNRS – Université de Lorraine, Campus ARTEM, 2 allée André Guinier, BP 50840, 54011 Nancy, France*

[2] *FZU – Institute of Physics of the Czech Academy of Sciences, Cukrovarnická 10/112, 162 00, Prague 6, Czech Republic*

[3] *Department of Materials Science and Engineering, Northwestern University, Evanston, IL-60208, USA*

[*]Corresponding author: christophe.candolfi@univ-lorraine.fr

Abstract

Chalcogenide semiconductors and semimetals continue to be of prime interest for thermoelectric applications in power generation. As another representative of this broad class of materials, tetragonal InTe has recently emerged as a promising candidate due to its very limited ability to transport heat leading to high thermoelectric performance near 800 K in polycrystalline samples. However, little is known on the basic physical mechanisms governing its electronic and thermal properties, an in-depth study of which requires the growth of single crystals. Here, we report a

detailed investigation of the transport properties of InTe single crystals grown by the Bridgman-Stockbarger technique over a wide range of temperatures (5 – 800 K). Except for the Hall coefficient that remains nearly isotropic below 300 K, all the transport coefficients show a significant anisotropy between the c and [110] direction of the crystal structure. In contrast to electronic band structure calculations suggesting a semimetallic ground state, the high-temperature dependence of the thermopower $\alpha(T)$ indicates that InTe is a semiconductor with a band gap estimated to be 0.26 eV from the Goldsmid-Sharp relation. Despite the absence of grain boundary scattering, an extremely low lattice thermal conductivity κ_{ph} of 0.32 W m^{-1} K^{-1} at ~ 780 K is achieved along the [110] direction. Remarkably, this value is equivalent to the glassy limit κ_{glass} based on phonon-mediated heat transport suggesting that, at high temperatures, the thermal transport in InTe has reached its minimum value. The combination of extremely low κ_{ph} values with a relatively high power factor yields a maximum dimensionless thermoelectric figure of merit *ZT* of 0.61 at 780 K along the [110] direction. The present study provides a solid basis for future doping strategies of InTe for high-temperature thermoelectric applications.

1. Introduction

Chalcogenide semiconductors and semimetals play a prominent role for applications in energy conversion.[1-3] They are notably used as the active parts in thermoelectric devices that efficiently and reliably convert waste heat into useful electrical energy and vice versa.[1,4-8] Their high thermoelectric performances originate from a favourable balance between good and easily-tuneable electronic properties and low thermal transport in spite of their simple crystal structures.[1,2,4] This combination of physical properties, challenging to meet, results in high

dimensionless thermoelectric figure of merit ZT defined as $ZT = \alpha^2 T/\rho(\kappa_e + \kappa_{ph})$ where α is the thermopower (or Seebeck coefficient), ρ is the electrical resistivity, T is the absolute temperature and κ_e and κ_{ph} are the electronic and lattice thermal conductivity, respectively.[1,4] Over the last few decades, several possible strategies have been applied for enhancing the ZT values by increasing the power factor (α^2/ρ) through either the introduction of magnetic ions[9-13] or band-structure engineering that includes band convergence, resonant level or energy-filtering effects,[14-23] or by decreasing the lattice thermal conductivity through nanostructuring or the formation of precipitated phases at various length scales.[24-27] All these strategies have successfully led to the design of highly-efficient thermoelectric materials, should it be for near-room-temperature refrigeration or high-temperature power generation.

Among the various binary chalcogenide semiconductors investigated so far,[1] InTe has received significantly less attention in comparison to other binary tellurides. Unlike PbTe that crystallizes in a cubic rocksalt structure,[1] InTe adopts a tetragonal unit cell under ambient pressure described in the *I*4/*mcm* space group (No. 140).[28-32] The crystal structure can be viewed as a stacking along the [110] direction of infinite linear chains of edge-sharing $(In^{3+}Te_4^{2-})^-$ tetrahedra running along the *c* axis. In^+ cations reside in large tunnels delimited by these chains and show marge thermal displacement parameters with a thermal ellipsoid elongated along the *c* axis (Figure 1).[28] Recent low-temperature X-ray diffraction measurements have suggested that In-rich samples of InTe undergo tetragonal-to-orthorhombic and orthorhombic–to-orthorhombic lattice distortions upon cooling below 185 and 87 K, respectively, with the latter possibly be accompanied by the formation of a charge density wave (CDW).[32]

Over the last decades, only few studies have been devoted to the study of the electronic and optical properties of single-crystalline InTe.[28-34] First reports on the transport properties have

indicated anisotropic electrical resistivity, carrier mobility and thermopower values along directions parallel and perpendicular to the *c* axis.[33] A positive α value of 630 μV K^{-1} was measured along a direction perpendicular to the natural cleavage plane, reported to be the (110) plane.[33] It is not until recently, however, that the thermoelectric properties of polycrystalline InTe were investigated in detail. Starting from intentionally In-deficient chemical compositions, Jana *et al*.[29] showed that the hole concentration depends on the nominal In concentration, suggesting the presence of acceptor-like In vacancies that lead to a stronger metallic character of transport compared to prior studies. One of the most remarkable properties of InTe is its extremely low κ_{ph} values that decrease to 0.30 W m^{-1} K^{-1} at 625 K.[29] As shown by recent inelastic neutron scattering experiments, the presence of distributions of low-energy optical modes, assigned to the dynamics of In^{+} cations that possibly experience a multiple-well potential, contributes to efficiently disrupt the propagation of acoustic phonons.[35] Owing to this low ability to transport heat and the possibility to tune the electronic properties via In deficiency, a maximum *ZT* of ~ 0.85 was obtained at 600 K.[29] Further subsequent attempts at doping InTe with Cd resulted in a similar peak *ZT* value (0.87 at 773 K).[36] However, all recent studies have focused on polycrystalline specimens with no detailed study dedicated to single-crystalline InTe.

Here, we report on a detailed investigation of the transport properties (5 – 800 K) of single-crystalline InTe measured along the *c* and [110] directions of the tetragonal unit cell. Low-temperature single-crystal X-ray diffraction performed down to 85 K did not evidence any lattice distortion. The temperature variations in α above 300 K are consistent with a semiconducting behaviour characterized by a band gap of 0.26 eV, in contrast with the semimetallic ground state suggested by electronic band structure calculations. Remarkably, κ_{ph} values are equivalent to those measured at high temperatures in polycrystalline samples, reaching the amorphous limit

determined by the model developed by Cahill and Pohl.[37] The combination of moderately high power factor α^2/ρ and extremely low κ_{ph} results in a maximum *ZT* value of 0.61 at 780 K along the [110] direction.

2. Experimental Section

2.1 Crystal growth

All the handlings and manipulations of the elements and ingots were performed in a dry, Ar-filled glove box. A large, centimetre-sized single crystal of InTe was synthesized using the conventional, unseeded Bridgman-Stockbarger method. The crystal growth was realized via a two-step process. As a first step, a polycrystalline ingot of InTe with a nominal composition of 50-50 was prepared by direct reaction of stoichiometric amounts of high-purity elemental In and Te (99.999 %, purchased from Alfa Aesar and 5N+, respectively) in a pre-evacuated, sealed silica tube with outer diameter of 18 mm and thickness of 1.5 mm. Once sealed under secondary vacuum, the tube was placed in a vertical rocking furnace and heated to 1023 K. After maintaining this temperature for 15 h, the tube was quenched in room-temperature water and subsequently opened inside the glove box. As a second step, the obtained ingot of ~15 cm in length and ~15 mm in diameter was introduced into a long silica tube (outer diameter of 18 mm and thickness of 1.5 mm) exhibiting a carefully-designed V-shaped end to reduce the number of seeded crystals at the beginning of the solidification. The tube was degassed overnight before being sealing under secondary vacuum. The sealed tube was then placed in a two-zone furnace for crystal growth. The first zone (top of the furnace) was kept at 1000 K while the electrical power of the second zone was kept off to let the

crystallization process occurs at a natural cooling rate. The pulling rate was maintained at a low value of 0.35 mm h^{-1} with a thermal gradient of around 10 – 15 K cm^{-1} near the solidification temperature. A low growth rate is usually necessary to achieve a stable growth and minimize constitutional supercooling. After 30 days, the furnace was switched off while the lowering of the tube was allowed for two additional days. The resulting ingot was ~11 cm in length, cleaved into two pieces along its characteristic cleavage plane, discussed in detail below. As mentioned in prior studies, the ingot tends to easily cleave yielding a mirror-like surface suggesting a single-crystalline nature. The experimental density of the ingot, determined from its weight and geometrical dimensions, was 6.23 g cm^{-3}. This value, in excellent agreement with the theoretical density of InTe determined from crystallographic data,[28] indicates a fully-dense ingot. Noteworthy, the ingot appeared to be very brittle and fragile, with a strong tendency to cleave along the (110) planes as determined by Laue diffraction. The (110) planes correspond to the planes running along the In^{+} cations residing in the tunnels (see Figure 1). One specificity that makes this structure distinct from layered compounds, such as for instance the canonical thermoelectric compound Bi_2Te_3, is that these planes do not solely exist along one direction but are present, due to the symmetry of the crystal structure, along two directions at 90° from each other.

2.2 Structural and chemical characterizations

The single-crystalline nature of the grown ingot was verified by Laue diffraction performed at 300 K. Structural and chemical characterizations were carried out by powder X-ray diffraction (PXRD) on crushed pieces of the single crystal and scanning electron microscopy (SEM) on a small cleaved single-crystalline piece. PXRD measurements were performed at 300 K using a Bruker D8

Advance diffractometer ($CuK\alpha_1$ radiation, $\lambda = 1.54056$ Å). Rietveld refinements against the PXRD data were performed using the FullProf software.[38] SEM analyses were carried out using a Quanta FEG 650 (FEI) instrument in backscattering electron mode (BSE) in order to evidence possible secondary phases. The spatial distribution of In and Te were further assessed by electron dispersive X-ray spectroscopy (EDXS).

The single crystal was cut using a diamond-wire saw into bar-shaped (typical dimensions of $8\times2\times2$ mm^3) and square-shaped ($6\times6\times2$ mm^3) samples for physical property measurements. All the samples were cut from the same part of the single crystal to avoid possible variations in the carrier concentration and hence, in the transport properties. Additional orientated single-crystalline pieces were taken for inelastic neutron scattering measurements, reported in our previous study.[35] Of note, cutting samples for transport properties measurements along the direction perpendicular to the cleavage plane was very challenging due to its tendency to systematically cleaves during the cutting process and to the presence of cleavage planes along two other directions as mentioned above. For this reason, the thermal conductivity could not be measured above room temperature along this direction. Hereafter, the samples cut along two directions, that is, along the *c* axis and within the basal *ab* plane of the tetragonal unit cell, will be referred to as [001] and [110], respectively.

2.3 Transport, thermodynamic and magnetic properties measurements

Electrical resistivity, thermopower and thermal conductivity were measured simultaneously at low temperatures (5 – 300 K) on the bar-shaped samples using the thermal transport option of a physical property measurement system (PPSM, Quantum Design). Good electrical and thermal contacts

were realized by attaching four copper leads using a low-melting point braze. Hall effect measurements were performed on the same bar-shaped samples in the same temperature range by a five-probe configuration using the AC transport option of the PPMS. The Hall resistivity ρ_H was determined from the antisymmetric component of the transverse electrical resistivity ρ_{xy} measured under magnetic fields $\mu_0 H$ ranging between –1 and +1T following the formula $\rho_H = \left[\rho_{xy}(+\mu_0 H) - \rho_{xy}(-\mu_0 H)\right]/2$. In this field range, the $\rho_H(\mu_0 H)$ curves were found to be linear over the entire temperature range. The Hall coefficient R_H was determined from the slope of the $\rho_H(\mu_0 H)$ data in the limit $\mu_0 H \to 0$. The Hall carrier concentration p_H and Hall mobility μ_H was calculated using the single-carrier relations $p_H = 1/R_H e$ and $\mu_H = R_H/\rho$, respectively, where e is the elementary charge. Of note, in anisotropic crystals, the galvanomagnetic properties are described by a tensor composed of several independent components.[39] Because InTe crystallizes in the tetragonal space group *I*4/*mcm*, the number of independent coefficients is limited to one along the *c* axis (along the cleavage plane) and one perpendicular to it (within the *ab* basal plane of the tetragonal unit cell). In principle, in such a case, the above-mentioned simple formulas relating p_H, μ_H and R_H cannot be used. However, as we shall see below, the anisotropy in the $R_H(T)$ data measured along both directions remains moderate in the present case, justifying the approximation used herein. The modelling of the transport data using expressions that are solutions to the Boltzmann transport equations has been performed by considering the values of p_H measured along the *c* direction. The conclusions drawn from this modelling would not be affected by using the values measured along the [110] direction. Field-cooled magnetization M measurements were performed between 5 and 300 K on a small single-crystalline piece of approximately 20 mg under an applied magnetic field of 2 T using a SQUID magnetometer (Quantum Design). Additional

isotherm $M(\mu_0 H)$ curves were collected between at 5, 150 and 300 K under magnetic fields ranging between –7 T and +7 T.

High-temperature thermopower and electrical resistivity were measured simultaneously in the temperature range 300 – 800 K on the bar-shaped samples using a ZEM-3 apparatus (Ulvac-Riko) using a conventional four-probe method under controlled inert atmosphere (He). Thermal diffusivity a was measured on the square-shaped sample (along the c axis) using a laser flash technique (Netzsch LFA 427) between 300 and 800 K. Prior to the measurement, the sample was polished and spray-coated with graphite to ensure a homogenous signal absorption and emission on the respective surfaces. The thermal conductivity of the sample was calculated using the relation $\kappa = aC_p d$ where C_p is the specific heat, measured experimental by differential scanning calorimetry between 300 and 800 K, and d is the experimental density of the sample assumed to be temperature-independent.

An overall good match between the low- and high-temperature data were observed at room temperature, except for the thermal conductivity due to the thermal radiations that tend to increase the measured values above ~ 200 K. The experimental uncertainty associated with these measurements is estimated to be 5% for all transport properties at low temperatures, 5% for the electrical resistivity and thermopower at high temperatures and 10% for the thermal conductivity. The combined uncertainty in the determination of the ZT values is thus estimated to be 17%.[40]

3. Results and discussion

3.1 Crystal structure and chemical homogeneity

The single-crystalline nature of the grown ingot (see the inset in Figure 2) was confirmed by Laue diffraction, which further showed that the natural cleavage plane corresponds to the (110) plane, that is, parallel to the *c* axis of the crystal structure, in agreement with early studies.[28,33] The growth axis was determined to be along the [111] direction. All the Laue patterns showed well-defined reflection spots indicating the good quality of our crystal (see the inset in Figure 2). Elemental X-ray mapping, performed on a cleaved surface, showed homogenous distributions of In and Te, revealing a good chemical homogeneity.

In agreement with literature data, both single-crystal X-ray diffraction and the PXRD pattern collected at 300 K on crushed single-crystalline pieces confirm that InTe crystallizes in a tetragonal unit cell described in the space group *I*4/*mcm* with the In1, In2 and Te atoms located on the 4*a* (0, 0, 1/4), 4*b* (0, 1/2, 1/4) and 8*h* (x = 0.18223(2), y = – 0.31777(2), 0) Wyckoff site, respectively. Of note, the relative intensities of the Bragg reflections observed in the PXRD pattern can be strongly renormalized due to the tendency of the crystallites to show some preferred orientation. This effect can be nevertheless mitigated by pouring the powders on the XRD sample holder without subsequently pressing them, as shown by the comparison of the patterns collected with and without pressing (Figure 2).

No evidence of the tetragonal-to-orthorhombic lattice distortion below 185 K reported previously was observed in the low-temperature single-crystal data down to 85 K.[32] In contrast, additional low-temperature PXRD experiments performed on crushed single-crystalline pieces

down to 115 K reveal the development of extra reflections (Figure 3) below about 200 K, signalling either a structural transition or a phase decomposition. This transformation is reversible as shown by PXRD patterns collected upon warming back to room temperature. Because several structural models can account for these additional reflections (see the ESI for a detailed discussion), no definitive conclusions as for the exact nature of this transition could be drawn from the present data. Further low-temperature microscopy and diffraction experiments will be helpful to elucidate the crystal structure of the low-temperature phase and the resulting microstructure of the sample.

3.2 Transport properties

The temperature dependences of the electrical resistivity ρ and thermopower α are shown in Figure 4a and 4b, respectively. In both crystallographic directions, InTe exhibits a metallic-like behaviour over the entire temperature range. Despite the single-crystalline nature of this sample, high residual ρ values of ~ 29.7 and 40.6 μΩm are reached at 5 K along the [110] and *c* directions, respectively. While the high ρ values measured in both directions may be suggestive of a rather low crystalline quality with a residual resistivity ratio ρ_{300K}/ρ_{5K} of ~2 and ~1 along the *c* and [110] directions, respectively, inelastic neutron scattering measurements performed on pieces taken from the same crystal have evidenced a mosaicity falling below the instrumental resolution, that is, below 0.1°, indicative of good crystalline quality.[35] These low ratios may thus reflect the significant impact of the rattling-like motion of the In^+ cations in the tunnels on the hole mobility, as observed in several rattler-containing compounds for which very low Hall mobility values have been reported.[41-43]

The low-temperature temperature dependence of ρ did not evidence any clear structural distortion around 185 K as suggested by the PXRD data. Moreover, no evident sign of lattice modulation that would accompany the formation of a CDW is observed near 87 K, in agreement with prior results obtained in a nearly-stoichiometric InTe sample.[32] Above room temperature, the ρ values increase upon warming from 24.4 μΩm and 77.8 μΩm at 300 K to 67.8 μΩm and 182.2 μΩm at ~ 785 K along the [110] and *c* directions, respectively. The $\rho(T)$ data evidence a clear anisotropy with an anisotropy ratio, defined as $\rho_{[001]}/\rho_{[110]}$, equal to ~ 3.2 at 300 K, which slightly decreases to ~ 2.7 near 785 K.

The positive α values measured in the entire temperature range indicates a *p*-type electrical conduction, in agreement with prior reports on both single-crystalline and polycrystalline InTe.[29-33] At low temperatures, $\alpha(T)$ is characterized by a weak, yet well-defined peak near 15 K suggestive of a phonon-drag contribution, akin to that observed in the PbTe or SnTe tellurides,[44,45] which is superimposed to the diffusive thermopower that dominates above 30 K. Consistent with $\rho(T)$, no evident sign of CDW transition is observed, which would originate from the restructuring of the Fermi surface due to the partial removal of density of states at the Fermi level on crossing the transition temperature.[46-48] This absence is consistent with prior results,[32] suggesting that a CDW seems to develop only in In-rich samples.

Above 300 K, α increases linearly with increasing temperature up to around 700 K where α values of 180 and 170 μV K^{-1} are achieved along the *c* and [110] directions, respectively. The α values tend to level off along the *c* direction, eventually peaking near 700 K before slightly decreasing upon further warming. In contrast, the α values measured in the [110] direction increase monotonically up to 780 K. A tendency towards levelling off is nevertheless discernible at the highest temperature measured, suggesting that a maximum would be likely observed at slightly

higher temperatures. The absence of a corresponding decrease in $\rho(T)$ that would be likely observable above 800 K is due to the differing expressions of the electrical resistivity and thermopower in a two-carrier regime, with the latter being a function of the partial electron and hole thermopowers weighed by the corresponding partial electrical conductivities. Thus, the onset temperature of the bipolar effect can slightly vary between these two transport properties.

The presence of a maximum in $\alpha(T)$ suggests that minority carriers start playing a prominent role above 700 K. Using the Goldsmid-Sharp relation $E_g = 2e\alpha_{max}T_{max}$,[49] which relates the thermal band gap E_g to the maximum thermopower value α_{max} reached at the peak temperature T_{max}, yields $E_g = 0.26$ eV. While consistent with optical absorption spectroscopy performed on polycrystalline InTe evidencing a band gap of 0.22 eV,[36] this value contrasts with the absence of a band gap predicted by electronic band structure calculations reported in prior studies.[29-32,35] These measurements thus suggest that InTe behaves as a narrow-band-gap semiconductor, with the metallic-like properties originating from small deviations from the nominal stoichiometry. The narrow, yet finite band gap width naturally explains the very high α values measured in early studies that were likely due to compensation effects leading to weakly-doped, nearly-intrinsic semiconducting properties.[33] The fact that semiconducting properties can be obtained in InTe is thus radically different from the case of SnTe for which the Sn vacancies can never be fully compensated by extrinsic doping.[50,51] The ease with which the defects in InTe may be compensated offers interesting prospects to further tune the α values through either doping or saturation annealing, as demonstrated in SnTe, Mg_3Sb_2 or PbTe.[52-58]

Interestingly, while $\alpha(T)$ is often found to be nearly isotropic in materials crystallizing with an anisotropic crystal structure, a clear and significant anisotropy persists over the entire temperature range in the present case. The trend observed between both directions is qualitatively

similar to that observed in the $\rho(T)$ data, that is, the highest ρ values correspond to the highest α values. This finding suggests an asymmetry in the electron-hole density-of-states effective masses due to asymmetric dispersions of the valence and conduction bands, in agreement with electronic band structure calculations.[29-32,35] The presence of a maximum in $\alpha(T)$ near 700 K in the *c* direction suggests that minority carriers start to contribute to the electrical transport above 700 K, which explains the steeper slopes $\partial\rho/\partial T$ observed above 600 K in both directions.

The Hall coefficient R_H is positive across the entire temperature range covered (Figure 5a), indicative of a dominant hole-like contribution, in agreement with the positive sign of α. The fact that the Hall resistivity ρ_H varies linearly with the applied magnetic field between –1 and +1T is likely due to the presence of a small amount of acceptor defects that shift the chemical potential inside the valence bands, making a hole-like signal the dominant contribution up to at least 300 K. In contrast to other transport coefficients that do not show clear signatures of the possible transition observed in the PXRD data, a clear anomaly is observed in the $R_H(T)$ data, peaking at 175 K along both directions. Intriguingly, this abnormal behaviour in $R_H(T)$ is similar to that observed by Back *et al*.[32] in a polycrystalline, nearly-stoichiometric sample, demonstrating the robustness of this observation regardless of the nature of the sample. This anomaly is particularly pronounced along the [110] direction, while still visible along the *c* direction near the same peak temperature, albeit with a significantly reduced amplitude and reversed effect. This difference suggests that the origin of this anomaly depends on the crystallographic direction. Nevertheless, the exact relationship between the possible phase transition and this anomaly remains to be fully elucidated (see ESI for possibilities).

The presence of a small amount of defects, ascribed to In vacancies, is consistent with the relatively high hole concentration p_H of ~ 7.5 $\times 10^{19}$ cm^{-3}. The nearly temperature-independence of

$R_H(T)$ is indicative of degenerate, metallic-like properties and the finite Sommerfeld coefficient γ derived from specific heat measurements down to ^{3}He temperatures.[28] The measured p_H value is comparable to those measured in pristine polycrystalline samples in prior studies.[29-32]

A significant anisotropy is observed in the Hall mobility μ_H that amounts to ~10 cm^2 V^{-1} s^{-1} and ~35 cm^2 V^{-1} s^{-1} along the *c* and [110] directions, respectively (Figure 5b) . The anisotropy ratio of 3.5 is consistent with that determined in prior reports on single-crystalline InTe [26]. As we will see below, the anisotropy in μ_H is partially due to the density-of-states effective masses not equivalent between both directions. However, fully elucidating the origin of the higher mobility measured along the [110] direction and determining whether InTe follows the general trend in the bonding mechanism observed in chalcogenide semiconductors will require detailed quantitative chemical bonding analysis.[59,60] In addition to the anomaly that impacts $R_H(T)$, the $\mu_H(T)$ dependences are suggestive of neutral impurity scattering that dominates below ~50 K ($\mu_H(T) \propto T^0$) followed by a slight but noticeable decrease on approaching 300 K that may be ascribed to the onset of acoustic phonon scattering for which $\mu_H(T) \propto T^{-3/2}$. This near-room-temperature behaviour differs from that observed in polycrystalline InTe samples alloyed with Sb.[31] In these alloys, $\mu_H(T)$ was found to increase with temperature from 300 up to 400 K mimicking ionized impurity scattering ($\mu_H(T) \propto T^{3/2}$). Above 400 K, a mixed regime with both acoustic phonon and intervalley scattering was observed up to 585 K, with the latter mechanism prevailing at higher temperatures in pristine InTe. Hence, as demonstrated in the Zintl phase Mg_3Sb_2 and in various chalcogenide semiconductors,[57,61] the presence of ionized impurity scattering in the above-mentioned polycrystalline samples is likely not an intrinsic behaviour and may be due to presence of energy barriers at the grain boundaries giving rise to the observed activated-like temperature dependence.

Combining the p_H and α data, the transport properties of InTe were further modelled using solutions to the Boltzmann transport equation. Figure 6 shows the Ioffe-Pisarenko plot at 300 K, with the literature data reported on single-crystalline and polycrystalline samples added for comparison purposes.[29-32] While the shape of the valence band and conduction bands near the M point and along the X – P direction are nearly parabolic, the less-dispersive band located at the Z point exhibits a more complicated shape. Nevertheless, as a first approximation, the theoretical relation $\alpha(p)$ was calculated by considering a single-parabolic band model, assuming that acoustic phonon scattering prevails near room temperature, as often observed in chalcogenide semiconductors.[2,62-67] In this model, α and p_H are given by the following expressions[68]

$$\alpha = \frac{k_B}{e}\left(\frac{(2+\lambda)F_{1+\lambda}(\eta)}{(1+\lambda)F_{\lambda}(\eta)} - \eta\right) \quad (1)$$

$$p_H = 4\pi\left(\frac{2m^*_{DOS}k_BT}{h^2}\right)^{\frac{3}{2}} F_{\frac{1}{2}}(\eta) \quad (2)$$

where k_B is the Boltzmann constant, h is the Planck constant, η is the reduced Fermi energy, m^*_{DOS} is the density-of-states effective mass, λ is the scattering parameter related to the dominant scattering mechanism ($\lambda = 0$ for acoustic phonon scattering) and $F_i(\eta)$ is the Fermi integral defined as

$$F_i(\eta) = \int_0^{\infty} \frac{\xi^i d\xi}{1 + e^{\xi - \eta}} \quad (3)$$

where ξ is the reduced energy of the charge carriers. Using the experimental α and p_H values, this model yields nearly equivalent density-of-states effective masses of 0.74 and 0.98m_e (m_e is the bare electron mass), along the [110] and c direction, respectively. These nearly equivalent, yet slightly different values of m^*_{DOS} are consistent with the slightly distorted hole pockets characterizing the Fermi surface of lightly-doped, p-type InTe.[29-32] The two theoretical curves also describe most of the data reported in prior studies.[27-30] Notable exceptions are two of the three points measured by Jana *et al*.[29] While the point near 6×10^{18} cm^{-3} is reasonably close to the theoretical curve, the point measured at 3.5×10^{20} cm^{-3} is not captured by this model. This deviation from the theoretical trend possibly signals the breakdown of the present model due to the contribution of other bands as in SnTe, which is the canonical example of such a behaviour.[44,67,68] Additional InTe samples with higher hole concentrations should be studied in order to clarify this point. The good agreement between the SPB model and the experimental points over nearly two orders of magnitude further show that non-parabolic effects associated with the shape of the valence band around the Z point can be neglected up to hole concentrations of ~7.5×10^{19} cm^{-3}.

Due to the relatively high ρ values measured in both directions, moderate values of the power factor α^2/ρ are achieved (Figure 7). The anisotropy observed in both ρ and α results in anisotropic power factors with an average anisotropy ratio of 2.4. A maximum value of 0.52 mW m^{-1} K^{-2} is achieved at ~ 600 K along the [110] direction. Above this temperature, the values tend to decrease with increasing temperature due to the increasing contribution of minority carrier excitations to $\alpha(T)$.

Figure 8 shows the temperature dependence of the total thermal conductivity κ. At low temperatures, $\kappa(T)$ is characterized by the presence of a well-defined dielectric maximum likely reached slightly below 5 K, indicative of the good crystalline quality of our sample. The low room-

temperature κ values of 1.2 and 0.7 W m^{-1} K^{-1} along the *c* and [110] direction, respectively, are slightly lower than those measured in polycrystalline samples.[29-32] This difference is consistent with the absence of grain boundary scattering acting as an additional source of phonon diffusion in single crystals. Along the [110] direction, κ further decreases to 0.46 W m^{-1} K^{-1} at 780 K, a value close to that obtained by Jana *et al*.[29] for polycrystalline InTe. The difference between the κ values measured along both directions corresponds to an anisotropic ratio of ~1.5.

The lattice thermal conductivity κ_{ph} was calculated by subtracting the electronic contribution using the Wiedemann-Franz law $\kappa_e = LT/\rho$ where L is the Lorenz number. The temperature dependence of L above 300 K has been estimated by the above-mentioned SPB model. κ_{ph} reaches an extremely low value of 0.32 W m^{-1} K^{-1} at 780 K along the [110] direction, in agreement with the studies on polycrystalline samples.[29-32] This value is equivalent to those measured in several Tl-based compounds and materials crystallizing with a complex unit cell.[71-74] Interestingly, these κ_{ph} values are similar to those measured in the zigzag layered binary In_2Te_5 , which have been attributed to the presence of resonant bonding within planar-coordinated Te structure units.[75] In contrast, inelastic neutron scattering experiments performed at 300 K on the present single-crystalline specimen of InTe have shown that the dynamics of the loosely-bound In^+ cations play an important role in shaping the low-energy part of the phonon spectrum.[35] The associated dispersionless, optical modes evaded direct observation, a characteristic ascribed to anharmonic broadening of their energy profiles. The resulting limited phase space available for acoustic phonons, well-defined over the entire Brillouin zone, is an important ingredient that helps to limit κ_{ph} to the measured values around room temperature.[35] The further significant decrease in κ_{ph} upon warming shows that propagative acoustic phonons are efficiently disrupted, possibly due to a strong increase in three-phonon processes and the impact of quartic anharmonicity, both of which

have been shown to explain the extremely low κ_{ph} values observed in several low-κ_{ph} materials such as, for instance, tetrahedrite minerals.[76]

Such low κ_{ph} values achieved at high temperatures in both single-crystalline and polycrystalline samples suggest that the phonon transport has reached the Ioffe-Regel limit for phonons, that is, when the average phonon mean free path is on the order of the interatomic distance.[77] This lower bound to the heat transport κ_{glass} was estimated to be 0.33 W m^{-1} K^{-1} using the high-temperature limit of the formula derived by Cahill and Pohl,[37] which adequately describes this limit in amorphous and strongly-disordered compounds

$$\kappa_{glass} = \frac{1}{2}\left(\frac{\pi}{6}\right)^{-1/3} k_B V^{-2/3}(2v_T + v_L) \quad (4)$$

where V is the average volume per atom, v_T and v_L are the transverse and longitudinal sound velocity, respectively. v_T and v_L were measured at room temperature using a pulse-echo method and found to be equal to 1750 and 2522 m s^{-1}, respectively, in good agreement with the average transverse and longitudinal sound velocities calculated by lattice dynamics calculations and with the transverse sound velocities measured from the slope of the acoustic phonon dispersions measured by inelastic neutron scattering.[35] The lowest κ_{ph} values measured above 700 K reach κ_{glass}. Interestingly, due to the uncertainty in the determination of the temperature dependence of the Lorenz number, the κ_{ph} values might fall below this limit, a finding only observed in a handful of ultralow thermal conductivity materials. In such a case, the high-temperature limit of κ_{ph} might be better described by the limit κ_{diff} that corresponds to a diffusive mechanism where atomic

vibrations carry heat by diffusion. In this approach, the heat transfer is mediated by diffusons, providing another estimation of the lower bound of κ_{ph} given by the expression[78]

$$\kappa_{diff} \approx 0.76 k_B V^{-2/3} \frac{1}{3}(2v_T + v_L) \quad (5)$$

Using the above-mentioned sound velocities, this formula yields $\kappa_{diff} = 0.21$ W m^{-1} K^{-1}. The intriguing possibility that InTe enters a diffusive regime at high temperatures will warrant further theoretical and experimental investigations.

The temperature dependence of the *ZT* values for both directions is shown in Figure 9a. Due to the relatively high power factor and, most notably, the extremely low thermal conductivity values, a peak *ZT* value of 0.61 has been achieved at ~780 K along the [110] direction. This value is lower than that obtained in polycrystalline samples due to the relatively high ρ values of the present crystal and the lower κ values achieved in polycrystalline samples.[29-32] The lower power factor achieved in the *c* direction than that obtained within the basal plane will result in lower *ZT* values. To determine the optimum hole concentration level, the theoretical dependence of the *ZT* values on the hole concentration has been calculated by the above-mentioned SPB model using the following expressions[4,68]

$$ZT = \frac{\alpha^2}{L + (\psi\beta)^{-1}} \quad (6)$$

$$\beta = \frac{\mu_0 (m^*/m_e)^{3/2} T^{5/2}}{\kappa_{ph}} \quad (7)$$

$$\psi = 2e\left(\frac{2\pi k_B m_e}{h^2}\right)^{3/2} \frac{F_\lambda(\eta)}{\Gamma(1+\lambda)} \tag{8}$$

where $\Gamma(x)$ is the gamma function and μ_0 is the intrinsic electron mobility determined from the Hall mobility μ_H

$$\mu_H = \mu_0 \frac{\sqrt{\pi} F_\lambda(\eta)}{2\Gamma(1+\lambda) F_{1/2}(\eta)} \tag{9}$$

In these calculations, the κ_{ph} values measured at 300 and 600 K were used while the hole concentration measured at 300 K was assumed to be constant up to 600 K. This analysis was not considered at temperatures higher than 600 K due to minority carrier effects that appear above this temperature, the influence of which is not taken into account in the SPB model. The comparison of the theoretical curves with the experimental *ZT* values (Figure 9b) shows that the present single-crystalline samples exhibit a nearly optimal hole concentration. Further optimization of the *ZT* values may nevertheless be achieved through substitutions on the In or Te sites that might yield higher mobility values, as observed in In-deficient polycrystalline samples.[29]

4. Conclusion

A large, centimetre-sized single crystal of InTe was successfully grown using the Bridgman-Stockbarger technique, allowing for a detailed investigation of its transport properties in the broad temperature range 5 – 800 K. Low-temperature powder X-ray diffraction evidenced a possible structural transition below 185 K. Measurements performed along the *c* axis and the [110] direction

show that the transport properties are anisotropic. Consistent with prior studies on polycrystalline samples, the as-grown single crystal is naturally *p*-type suggesting the presence of a small concentration of defects, possibility due to In vacancies. A clear anomaly in the Hall coefficient $R_H(T)$ was observed near 175 K and seems to be dependent on the crystalline orientation. This anomaly, which does not leave any corresponding fingerprints in the temperature dependences of the other transport coefficients and of the magnetization curves, will require further investigation to determine its nature. A remarkable property that characterizes InTe are the extremely low lattice thermal conductivity values measured along the [110] direction, falling down to a value as low as 0.32 W m^{-1} K^{-1} at 780 K, equivalent to the amorphous limit. The combination of relatively high power factors and low thermal conductivity values result in a maximum *ZT* value of 0.61 at 780 K along the [110] direction. Future studies of the possibility to tune the electronic properties by substitutions on the In or Te sites will be of interest to further enhance the thermoelectric performance by compensating the intrinsic defects and possibly reach pure semiconducting-like properties. In addition, applying the saturation-annealing technique will be helpful to better control the hole concentration and map the boundaries of off-stoichiometry on both the In- and Te-rich sides of the solidus. Finally, the fact that single crystals of InTe easily cleave along the (110) plane might make them suitable for exfoliation and further detailed investigations using surface-sensitive spectroscopy techniques.

Acknowledgments

P. L. and J. H. acknowledges the financial support of the Czech Science Foundation (project 18-12761S). Experiments were performed in MGML (mgml.eu), which is supported within the program of Czech Research Infrastructures (project no. LM2018096).

Conflict of Interest

The authors declare no conflict of interest.

References

[1] D. M. Rowe, *Thermoelectrics and its Energy Harvesting*, CRC Press, Boca Raton, FL, 2012.

[2] Y. Yu, M. Cagnoni, O. Cojocaru-Mirédin and M. Wuttig, *Adv. Funct. Mater*., 2020, **30**, 1904862.

[3] R. Woods-Robinson, Y. Han, H. Zhang, T. Ablekim, I. Khan, K. A. Persson and A. Kutayev, *Chem. Rev*., 2020, **120**, 4007–4055.

[4] H. J. Goldsmid, *Thermoelectric Refrigeration*. Springer, New York, USA, 1964.

[5] R. He, G. Schierning and K. Nielsch, *Adv. Mater. Technol*., 2018, **3**, 1700256.

[6] S. El Oualid, F. Kosior, A. Dauscher, C. Candolfi, G. Span, E. Mehmedovic, J. Paris and B. Lenoir, *Energy Environ. Sci.*, 2020, **13**, 3579–3591.

[7] L. E. Bell, *Science*, 2008, **321**, 1457–1461.

[8] I. Petsagkourakis, K. Tybrandt, X. Crispin, I. Ohkubo, N. Satoh and T. Mori, *Sci. Tech. Adv. Mater.*, 2018, **19**, 836–862.

[9] F. Ahmed, N. Tsujii and T. Mori, *J. Mater. Chem. A*, 2017, **5**, 7545–7554.

[10] J.-B. Vaney, S. Aminorroaya Yamini, H. Takaki, K. Kobayashi, N. Kobayashi and T. Mori, *Mater. Today Phys.*, 2019, **9**, 100090.

[11] N. Tsujii, A. Nishide, J. Hayakawa and T. Mori, *Sci. Adv.*, 2019, **5**, eaat5935.

[12] Y. Zheng, T. Lu, Md M. H Polash, M. Rasoulianboroujeni, N. Liu, M. E. Manley, Y. Deng, P. J. Sun, X. L. Chen, R. P. Hermann, D. Vashaee, J. P. Heremans and H. Zhao, *Sci. Adv.*, 2019, **5**, eaat9461.

[13] R. Ang, A. U. Khan, N. Tsujii, K. Takai, R. Nakamura and T. Mori, *Angew. Chem. Int. Ed.* 2015, **54**, 12909–12913.

[14] Y. Pei, X. Shi, A. LaLonde, H. Wang, L. Chen and G. J. Snyder, *Nature,* 2011, **473**, 66–69.

[15] J. Zhang, R. Liu, N. Cheng, Y. Zhang, J. Yang, C. Uher, X. Shi, L. Chen and W. Zhang, *Adv. Mater*., 2014, **26**, 3848–3853.

[16] K. H. Lee, S. Kim, H. S. Kim and S. W. Kim, *ACS Appl. Energy Mater*., 2020, **3**, 2214–2223.

[17] C M. Jaworski, V. Kulbachinskii and J. P. Heremans, *Phys. Rev. B*, 2009, **80**, 233201.

[18] J. P. Heremans, V. Jovovic, E. S. Toberer, A. Saramat, K. Kurosaki, A. Charoenphakdee, S. Yamanaka and G. J. Snyder, *Science*, 2008, **321**, 554–557.

[19] J, P. Heremans, B. Wiendlocha and A.M. Chamoire, *Energy Environ. Sci*., 2012, **5**, 5510–5530.

[20] S. Misra, B. Wiendlocha, J. Tobola, F. Fesquet, A. Dauscher, B. Lenoir and C. Candolfi, *J. Mater. Chem. C*, 2020, **8**, 977–988.

[21] B. Wiendlocha, J. B. Vaney, C. Candolfi, A. Dauscher, B. Lenoir and J. Tobola, *Phys. Chem. Chem. Phys*.. 2018, **20**, 12948–12957.

[22] K. T. Wojciechowski, T. Parashchuk, B. Wiendlocha, O. Cherniushok and Z. Dashevsky, *J. Mater. Chem. C*, 2020, **8**, 13270–13285.

[23] M. Kriener, M. Sakano, M. Kamitani, M. S. Bahramy, R. Yukawa, K. Horiba, H. Kumigashira, K. Ishizaka, Y. Tokura and Y. Taguchi, *Phys. Rev. Lett*., 2020, **124**, 047002.

[24] Y. Pei, N. A. Heinz, A. LaLonde and G. J. Snyder, *Energy Environ. Sci*. 2011, **4**, 3640–3645.

[25] J. Ma, O. Delaire, A. F. May, C. E. Carlton, M. A. McGuire, L. H. VanBebber, D. L. Abernathy, G. Ehlers, T. Hong, A. Huq, W. Tian, V. M. Keppens, Y. Shao-Horn and B. C. Sales, *Nature Nanotech*., 2013, **8**, 445–451.

[26] Y. Pei, J. Lensch-Falk, E. S. Toberer, D. L. Medlin and G. J. Snyder, *Adv. Funct. Mater*., 2011, **21**, 241–249.

[27] L. You, Y. Liu, X. Li, P. Nan, B. Ge, Y. Jiang, P. Luo, S. Pan, Y. Pei, W. Zhang, G. J. Snyder, J. Yang, Y. Zhang and J. Luo, *Energy Environ. Sci*., 2018, **11**, 1848–1858.

[28] T. Chattopadhyay, R. P. Santandrea and H. G. von Schnering, *J. Phys. Chem. Solids*, 1985, **46**, 351–356.

[29] M. K. Jana, K. Pal, U. V. Waghmare and K. Biswas, *Angew. Chem*., 2016, **55**, 7792–7796.

[30] S. Y. Back, H. Cho, Y. K. Kim, S. Byeon, H. Jin, K. Koumoto and J. S. Rhyee, *AIP Adv*., 2018, **8**, 115227.

[31] H. Zhu, B. Zhang, G. Wang, K. Peng, Y. Yan, Q. Zhang, X. Han, G. Wang, X. Lu and X. Zhou, *J. Mater. Chem. A*, 2019, **7**, 11690–11698.

[32] S. Y. Back, Y. K. Kim, H. Cho, M. K. Han, S. J. Kim and J. S. Rhyee, *ACS Appl. Energy Mater*., 2020, **3**, 3628–3636.

[33] S. Pal and D. N. Bose, *Solid State Commun*., 1996, **97**, 725–729.

[34] M. A. Nizametdinova, *Phys. Stat. Sol. (b),* 1980, **97**, K9–K12.

[35] S. Misra, C. Barreteau, J. C. Crivello, V. M. Giordano, J. Castellan, Y. Sidis, P. Levinský, J. Hejtmánek, B. Malaman, A. Dauscher, B. Lenoir, C. Candolfi and S. Pailhès, *Phys. Rev. Research*, 2020, **2**, 043371.

[36] S. Pan, H. Liu, Z. Li, L. You, S. Dai, J. Yang, K. Guo and J. Luo, *J. Alloy Compd.,* 2020, **813**, 152210.

[37] D. G. Cahill, S. K. Watson and R. O. Pohl, *Phys. Rev. B*. 1992, **46**, 6131–6140.

[38] J. Rodriguez-Carvajal, *Physica B*., 1993, **192**, 55–69.

[39] Y. C. Akgöz and G. A. Saunders, *J. Phys. C: Solid State Phys*., 1975, **8**, 1387–1396.

[40] E. Alleno, D. Bérardan, C. Byl, C. Candolfi, R. Daou, R. Decourt, E. Guilmeau, S. Hébert, J. Hejtmanek, B. Lenoir, P. Masschelein, V. Ohorodniichuk, M. Pollet, S. Populoh, D. Ravot, O. Rouleau and A. M. Soulier, *Rev. Sci. Instrum*., 2015, **86**, 011301.

[41] H. Lin, G. Tan, J. N. Shen, S. Hao, L. M. Wu, N. Calta, C. Malliakas, S. Wang, C. Uher, C. Wolverton and M. G. Kanatzidis, *Angew. Chem*., 2016, **55**, 11431–11436.

[42] Y. Jiang, F. Jia, L. Chen and L. M. Wu, *ACS Appl. Mater. Interfaces*, 2019, **11**, 36616–36625.

[43] D. J. Safarik, T. Klimczuk, A. Llobet, D. D. Byler, J. C. Lashley, J. R. O'Brien and N. R. Diley, *Phys. Rev. B*, 2012, **85**, 014103.

[44] D. Ibrahim, C. Candolfi, S. Migot, J. Ghanbaja, A. Dauscher, G. Le Caër, B. Malaman, C. Semprimoschnig and B. Lenoir, *Phys. Rev. Mater*., 2019, **3**, 085404.

[45] C. M. Jaworski, M. D. Nielsen, H. Wang, S. N. Girard, W. Cai, W. D. Porter, M. Kanatzidis and J. P. Heremans, *Phys. Rev. B,* 2013, **87**, 045203.

[46] C. Candolfi, M. Míšek, P. Gougeon, R. Al Rahal Al Orabi, P. Gall, R. Gautier, S. Migot, J. Ghanbaja, J. Kaštil, P. Levinský, J. Hejtmánek, A. Dauscher, B. Malaman and B. Lenoir, *Phys. Rev. B*, 2019, **101**, 134521.

[47] T. Gruner, D. Jang, Z. Huesges, R. Cardoso-Gil, G. H. Fecher, M. M. Koza, O. Stockert, A. P. Mackenzie, M. Brando and C. Geibel, *Nat. Phys*., 2017, **13**, 967–972.

[48] C. N. Kuo, W. Chen, C. Tseng, C. Hsu, R. Huang, F. Chou, Y. Kuo and C. Lue, *Phys. Rev. B*, 2018, **97**, 094101.

[49] H. J. Goldsmid and J. W. Sharp, *J. Electron. Mater*., 1999, **28**, 869–872.

[50] R. Moshwan, L. Yang, J. Zou and Z. Chen, *Adv. Funct. Mater*., 2017, **27**, 1703278.

[51] W. Li, Y. Wu, S. Lin, Z. Chen, J. Li, X. Zhang, L. Zheng and Y. Pei, *ACS Energy Lett*., 2017, **2**, 2349–2355.

[52] J. P. Fleurial, l. Gailliard, R. Triboulet, H. Scherrer and S. Scherrer, *J. Phys. Chem. Solids,* 1988, **49**, 1237–1247.

[53] R. F. Brebrick, *J. Phys. Chem. Solids*, 1969, **30**, 719–731.

[54] R. F. Brebrick and E. Gubner, *J. Chem. Phys*., 1962, **36**, 1283–1289.

[55] C. Hewes, M. Adler and S. Senturia, *J. Appl. Phys*., 1973, **44**, 1327–1332.

[56] D. Ibrahim, S. Misra, S. Migot, J. Ghanbaja, A. Dauscher, B. Malaman, C. Semprimoschnig, C. Candolfi and B. Lenoir, *RSC Advances,* 2020, **10**, 5996–6005.

[57] K. Imasato, C. Fu, Y. Pan, M. Wood, J. J. Kuo, C. Felser and G. J. Snyder, *Adv. Mater*., 2020, **32**, 1908218.

[58] J. Male, M. T. Agne, A. Goyal, S. Anand, I. T. Witting, V. Stevanovic and G. J. Snyder, *Mater. Horiz*., 2019, **6**, 1444–1453.

[59] Y. Yu, M. Cagnoni, O. Cojocaru-Mirédin and M. Wuttig, *Adv. Funct. Mater.*, 2020, **30**, 1904862.

[60] J. Zhang, L. Song, M. Sist, K. Tolborg and B. B. Iversen, *Nat. Commun.*, 2018, **9**, 4716.

[61] T. J. Slade, J. A. Grovogui, J. J. Kuo, S. Anand, T. P. Bailey, M. Wood, C. Uher, G. J. Snyder, V. P. Dravid and M. G. Kanatzidis, *Energy Environ. Sci*., 2020, **13**, 1509–1518.

[62] X. L. Shi, J. Zou and Z. G. Chen, *Chem. Rev*., 2020, **120**, 7399–7515.

[63] Y. Pei, H. Wang and G. J. Snyder, *Adv. Mater*., 2012, **24**, 6125–6135.

[64] H. Wang, E. Schechtel, Y. Pei and G. J. Snyder, *Adv. Energy Mater*., 2013, **3**, 488–495.

[65] C. L. Chen, H. Wang, Y. Chen, T. Day and G. J. Snyder, *J. Mater. Chem. A*, 2014, **2**, 11171–11176.

[66] C. Barreteau, D. Bérardan, E. Amzallag, L. Zhao and N. Dragoe, *Chem. Mater*., 2012, **24**, 3168–3178.

[67] P. K. Ventrapati, S. Misra, G. Delaizir, A. Dauscher, B. Lenoir and C. Candolfi, *J. Mater. Chem. C*, 2020, **8**, 14037–14048.

[68] V. I. Fistul, *Heavily Doped Semiconductors*, Plenum Press, New York, 1969.

[69] R. F. Brebrick and A. J. Strauss, *Phys. Rev*., 1963, **131**, 104–110.

[70] R. F. Brebrick, *J. Phys. Chem*. *Solids*, 1963, **24**, 27–36.

[71] R. Al Rahal Al Orabi, P. Gougeon, P. Gall, B. Fontaine, R. Gautier, M. Colin, C. Candolfi, A. Dauscher, J. Hejtmanek, B. Malaman and B. Lenoir, *Inorg. Chem*., 2014, **53**, 11699–11709.

[72] S. Yamanaka, K. Kurosaki, A. Kosuga, K. Goto, H. Muta, *MRS Symp. Proc*., 2006, **886**, 337−341.

[73] K. Kurosaki, A. Kosuga, H. Muta, M. Uno and S. Yamanaka, *Appl. Phys. Lett*., 2005, **87**, 061919.

[74] B. Wolfing, C. Kloc and J. Teubner, *Phys. Rev. Lett*., 2001, **86**, 4350−4353.

[75] W. Zhang, N. Sato, K. Tobita, K. Kimura and T. Mori, *Chem. Mater.*, 2020, **32**, 5335–5342.

[76] Y. Xia, V. Ozolins and C. Wolverton, *Phys. Rev. Lett*., 2020, **125**, 085901.

[77] A. F. Ioffe and A. R. Regel, *Prog. Semicond*., 1960, **4**, 237–291.

[78] M. T. Agne, R. Hanus and G. J. Snyder, *Energy Environ. Sci*., 2018, **11**, 609–616.

Figure captions

Figure 1. a) Perspective view of the crystal structure of InTe highlighting the edge-sharing chains of $(In^{3+}Te_4^{2-})^-$ tetrahedra shown in grey. The In1 (In^+), In2 (In^{3+}) and Te atoms are represented by blue, green and red spheres, respectively. The thermal ellipsoids are shown at the 95% probability level. The light blue lattice plane corresponds to the (110) cleavage plane. b) Perspective view showing the elongated thermal ellipsoids of the In^+ cations residing in the large tunnels delimited by the tetrahedra chains.

Figure 2. Powder X-ray diffraction pattern collected on crushed pieces of the single-crystal of InTe a) with and b) without pressing the powders on the sample holder. The upper right insets show a photograph of a piece of the Bridgman-grown single crystal, highlighting the (110) cleavage planes on the right side of the crystal and the Laue diffraction pattern obtained on the (110) cleavage plane with the theoretical reflections, shown in red, superimposed.

Figure 3. Temperature-dependent powder X-ray diffraction pattern measured on crushed pieces of the single-crystal of InTe upon cooling from 300 K to 115 K and, then, warming back to 300 K. The extra reflections that appear at low temperatures are marked by an asterisk.

Figure 4. Temperature dependence of a) electrical resistivity ρ and b) thermopower α measured along the *c* and [110] directions.

Figure 5. a) Temperature dependence of the a) Hall coefficient R_H and b) Hall mobility μ_H measured along the *c* and [110] directions. The anomalies observed for both directions around 175 K remain to be fully elucidated in future studies.

Figure 6. Ioffe-Pisarenko plot showing the variations in the thermopower α as a function of the hole concentration p_H. The experimental data were measured along the *c* and [110] directions. The black solid and dashed curves represent the theoretical dependence calculated using a single parabolic band model with acoustic phonon scattering and density-of-states effective masses of 0.74 and $0.98m_e$, respectively. Data from the literature, measured on polycrystalline and single-crystalline samples, have been added for comparison purposes (Jana *et al*. Ref. 29; Back *et al*. Ref. 32; Pal *et al*. Ref. 33).

Figure 7. Temperature dependence of the power factor $P = \alpha^2/\rho$ measured along the *c* and [110] directions.

Figure 8. a) Temperature dependence of the total thermal conductivity κ and b) high-temperature dependence of the lattice thermal conductivity κ_{ph} measured along the [110] and *c* directions.

Figure 9. a) Temperature dependence of the dimensionless thermoelectric figure of merit *ZT* for single-crystalline InTe along the [110] and *c* directions. b) Hole dependence of the *ZT* values calculated using the SPB model at 300 (solid red curve) and 600 K (blue dashed curve) along the [110] direction. Error bars corresponding to the experimental uncertainties (5% for Hall effect and 17% for *ZT*) have been added.

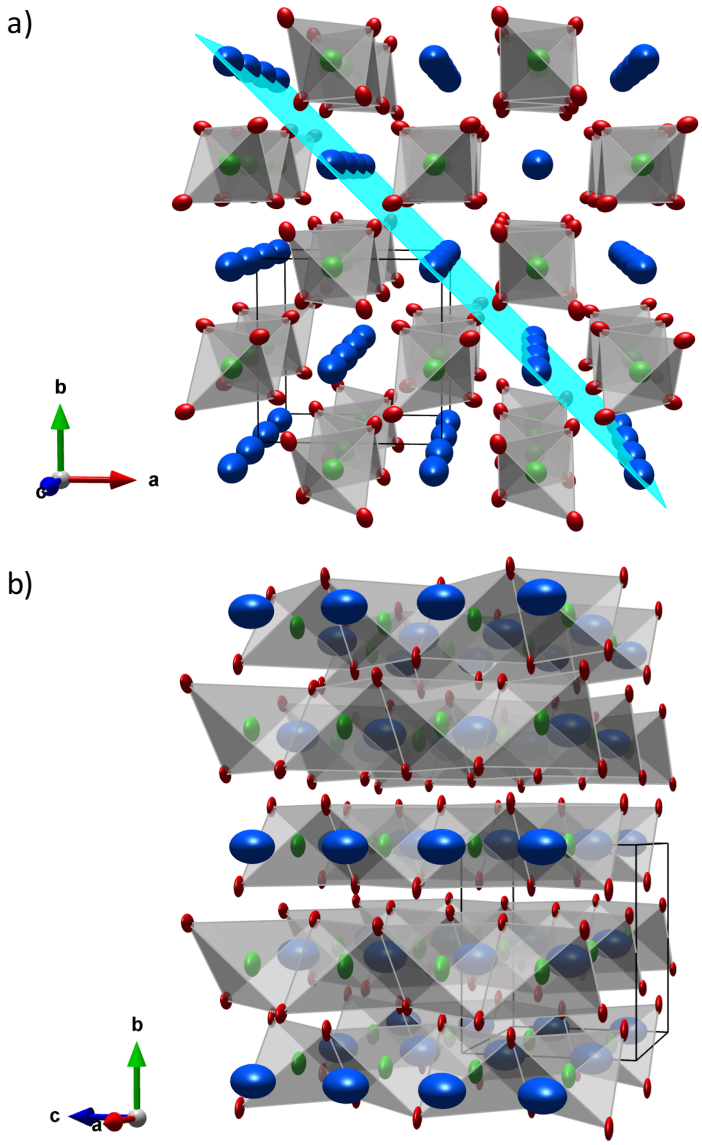

Figure 1

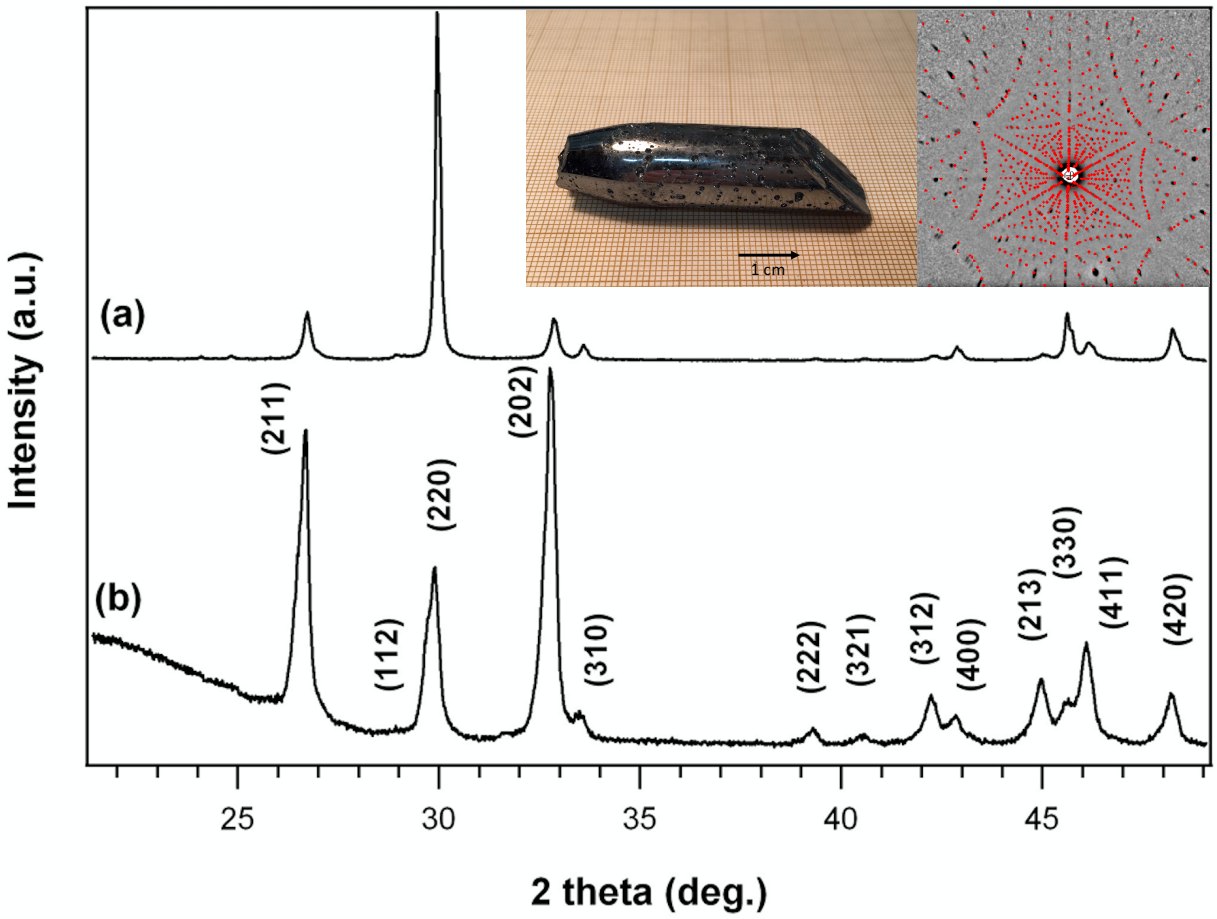
Intensity (a.u.)
(a)
(b)
(211)
(112)
(220)
(202)
(310)
(222)
(321)
(312)
(400)
(213)
(330)
(411)
(420)
1 cm
25
30
35
40
45
2 theta (deg.)

Figure 2

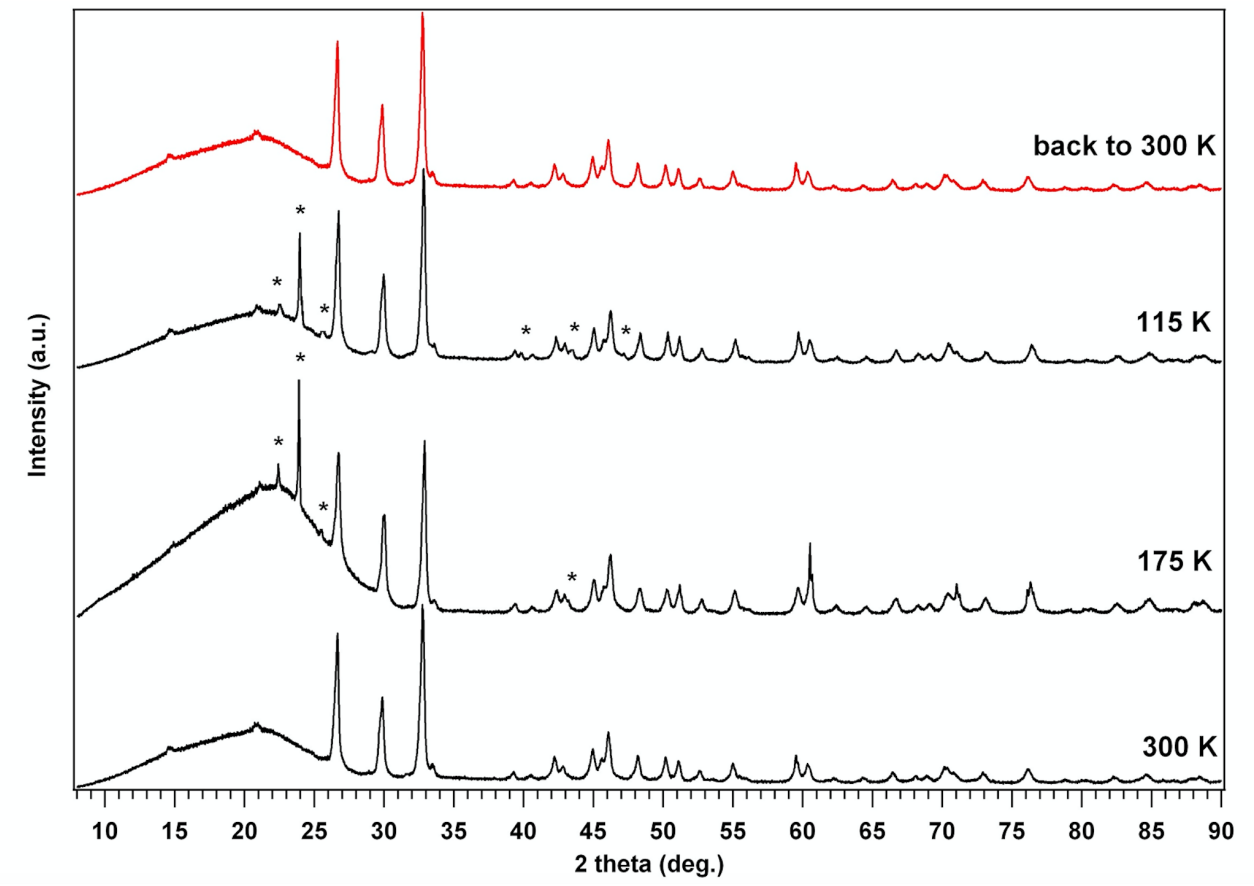
back to 300 K
115 K
175 K
300 K
Intensity (a.u.)
10 15 20 25 30 35 40 45 50 55 60 65 70 75 80 85 90
2 theta (deg.)

Figure 3

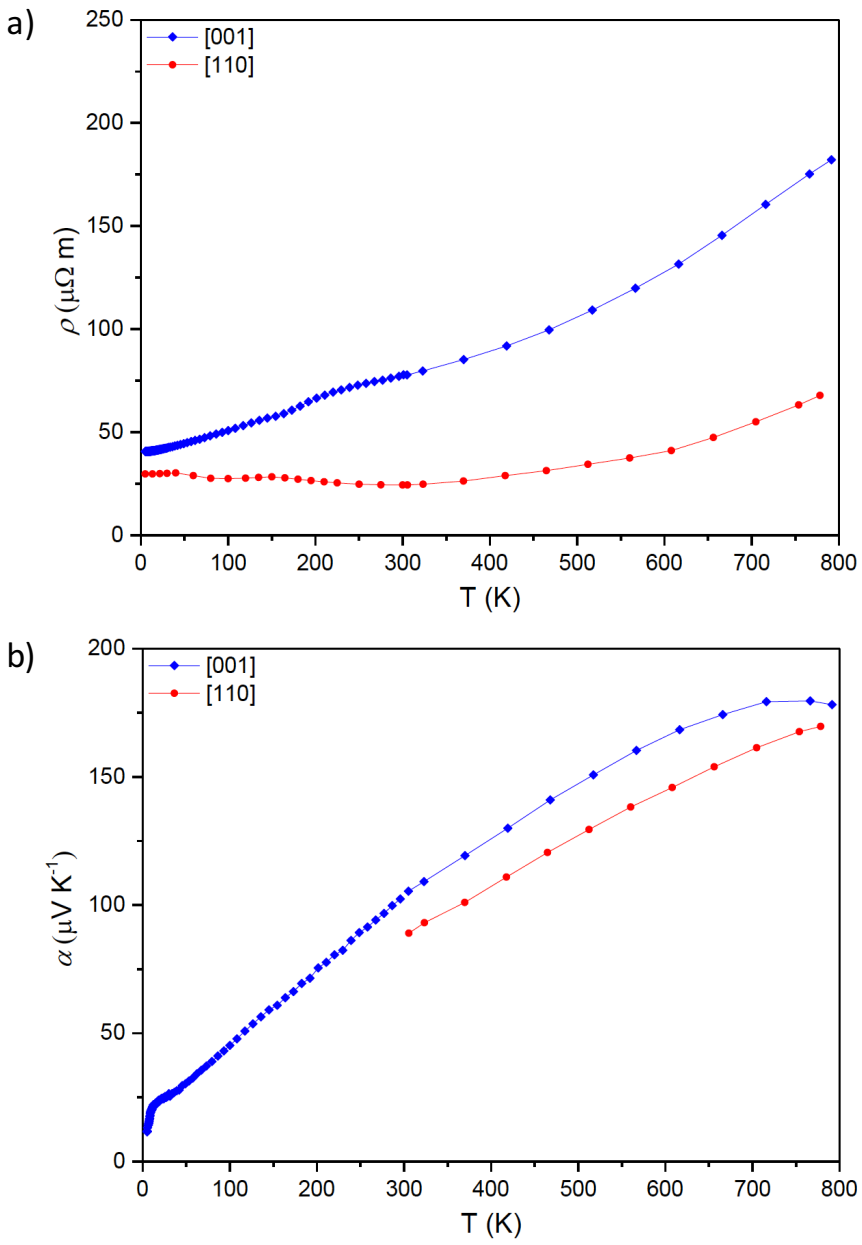

Figure 4

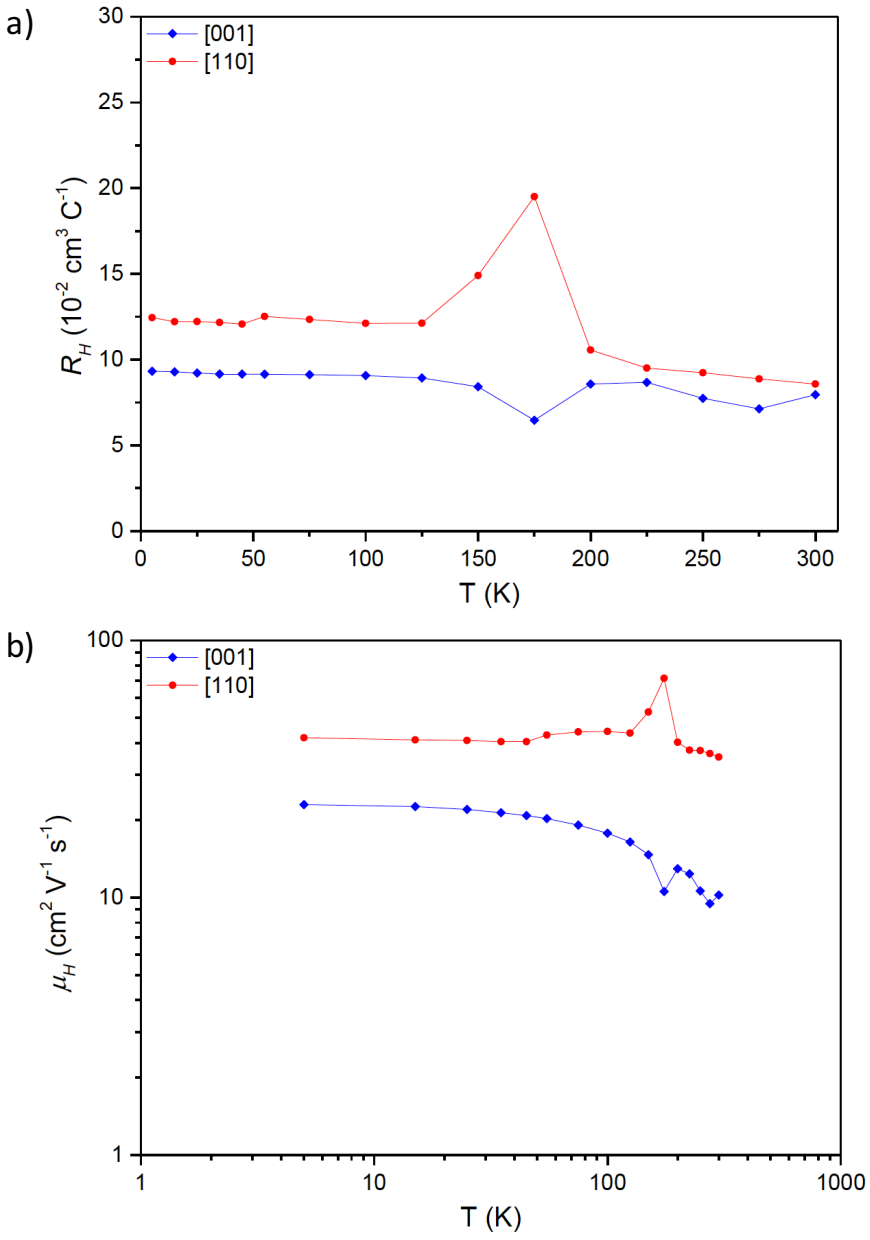

Figure 5

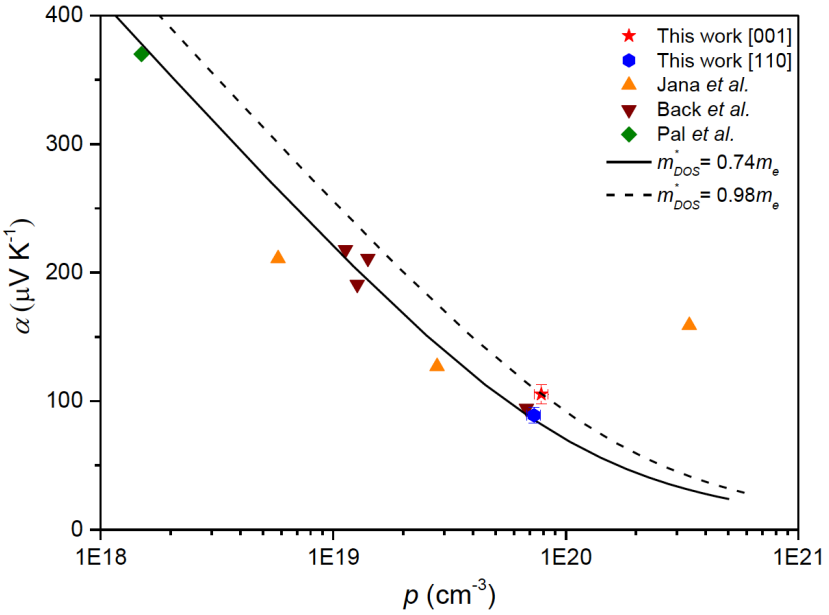
400
300
200
100
0
α (μV K-1)
1E18
1E19
1E20
1E21
p (cm-3)
This work [001]
This work [110]
Jana et al.
Back et al.
Pal et al.
m*DOS= 0.74me
m*DOS= 0.98me

Figure 6

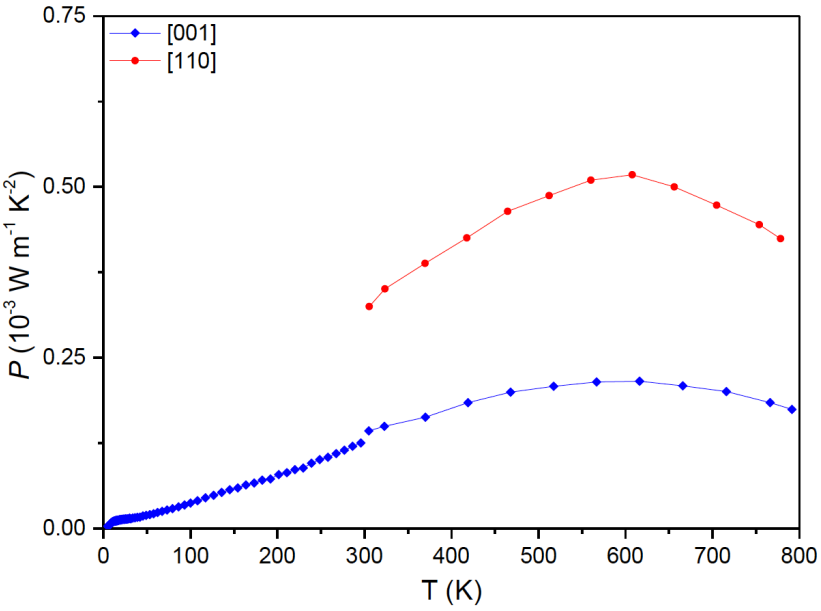
0.75
0.50
0.25
0.00
[001]
[110]
P (10-3 W m-1 K-2)
0
100
200
300
400
500
600
700
800
T (K)

Figure 7

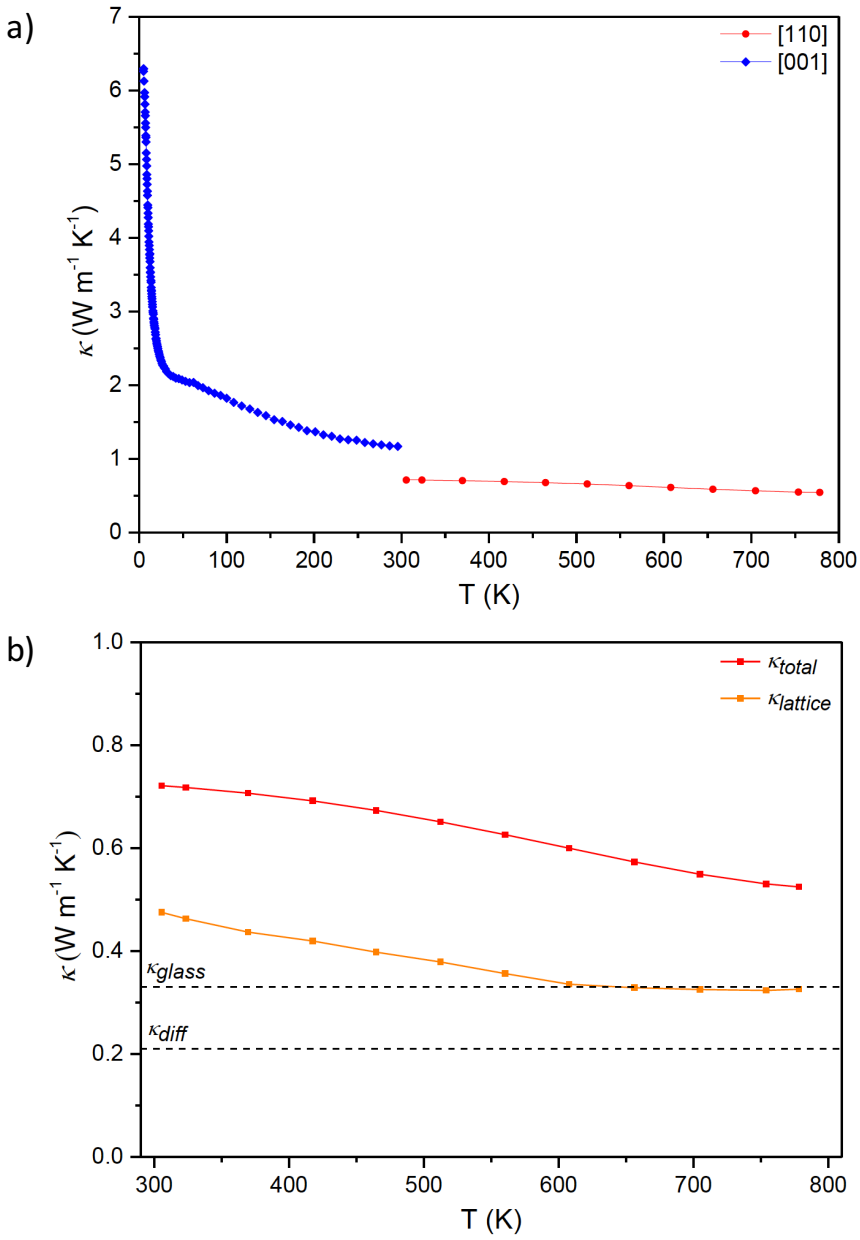

Figure 8

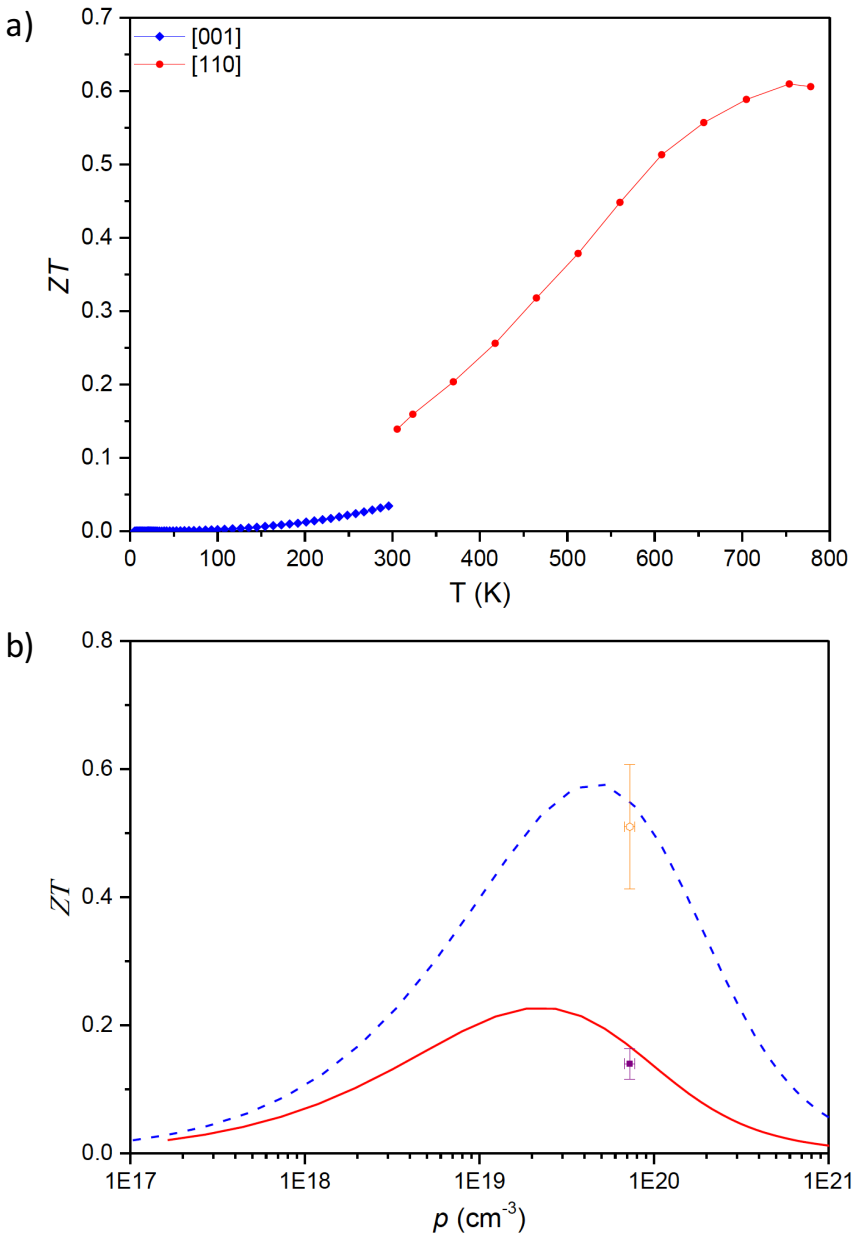

Figure 9